IOP Publishing and International Atomic Energy Agency Nuclear Fusion
Nucl. Fusion **47** (2007) 499–509 doi:10.1088/0029-5515/47/7/001

Confinement and local transport in the National Spherical Torus Experiment (NSTX)

S.M. Kaye[1], F.M. Levinton[2], D. Stutman[3], K. Tritz[3], H. Yuh[2], M.G. Bell[1], R.E. Bell[1], C.W. Domier[4], D. Gates[1], W. Horton[5], J. Kim[5], B.P. LeBlanc[1], N.C. Luhmann Jr[4], R. Maingi[6], E. Mazzucato[1], J.E. Menard[1], D. Mikkelsen[1], D. Mueller[1], H. Park[1], G. Rewoldt[1], S.A. Sabbagh[7], D.R. Smith[1] and W. Wang[1]

[1] Princeton Plasma Physics Laboratory, Princeton University, Princeton, NJ 08543, USA
[2] Nova Photonics Inc., Princeton, NJ 08540, USA
[3] The Johns Hopkins University, Baltimore, MD 21218, USA
[4] University of California, Davis, CA 95616, USA
[5] Institute for Fusion Studies, University of Texas, Austin, TX 78712, USA
[6] Oak Ridge National Laboratory, Oak Ridge, TN 37831, USA
[7] Department of Applied Physics, Columbia University, NYC, NY, 10027, USA

E-mail: skaye@pppl.gov

Received 18 December 2006, accepted for publication 3 April 2007
Published 13 June 2007
Online at stacks.iop.org/NF/47/499

Abstract
The NSTX operates at low aspect ratio (R/a∼1.3) and high beta (up to 40%), allowing tests of global confinement and local transport properties that have been established from higher aspect ratio devices. The NSTX plasmas are heated by up to 7 MW of deuterium neutral beams with preferential electron heating as expected for ITER. Confinement scaling studies indicate a strong B_T dependence, with a current dependence that is weaker than that observed at higher aspect ratio. Dimensionless scaling experiments indicate a strong increase in confinement with decreasing collisionality and a weak degradation with beta. The increase in confinement with B_T is due to reduced transport in the electron channel, while the improvement with plasma current is due to reduced transport in the ion channel related to the decrease in the neoclassical transport level. Improved electron confinement has been observed in plasmas with strong reversed magnetic shear, showing the existence of an electron internal transport barrier (eITB). The development of the eITB may be associated with a reduction in the growth of microtearing modes in the plasma core. Perturbative studies show that while L-mode plasmas with reversed magnetic shear and an eITB exhibit slow changes in L_{T_e} across the profile after the pellet injection, H-mode plasmas with a monotonic q-profile and no eITB show no change in this parameter after pellet injection, indicating the existence of a critical gradient that may be related to the q-profile. Both linear and non-linear simulations indicate the potential importance of electron temperature gradient (ETG) modes at the lowest B_T. Localized measurements of high-k fluctuations exhibit a sharp decrease in signal amplitude levels across the L–H transition, associated with a decrease in both ion and electron transport, and a decrease in calculated linear microinstability growth rates across a wide k-range, from the ion temperature gradient/TEM regime up to the ETG regime.

PACS numbers: 52.55.Fa, 52.25.Fi, 52.30.Gz

(Some figures in this article are in colour only in the electronic version)

1. Introduction

The National Spherical Torus Experiment (NSTX) provides a unique view into plasma transport and turbulence properties by operating at high toroidicity (low aspect ratio) with $R/a \simeq 1.3$, high β_T (up to 40%) and low collisionality [1, 2]. This is accomplished with up to 7 MW of ≃90 keV deuterium neutral beam injection power into deuterium plasmas in either the lower single null or the double null configuration. The NSTX operates at low toroidal field ($B_T = 0.35$–0.55 T) and relatively

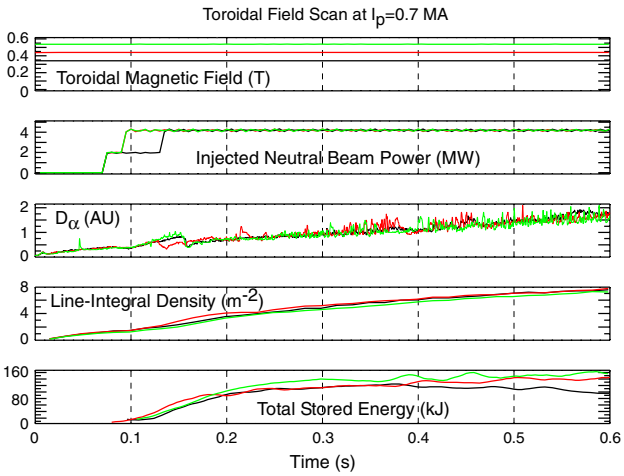

Figure 1. Overview of toroidal field scan at $I_p = 0.7$ MA. Plotted are toroidal field levels (0.35, 0.45 and 0.55 T) along with beam power in the top panel, the D_α trace in the middle panel, indicating all three B_T levels were H-mode discharges with small ELMs, and the line-integral density in the bottom panel, showing comparable densities for all three toroidal fields.

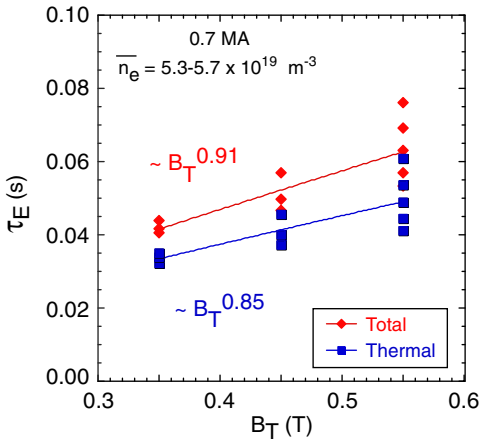

Figure 2. Total (red) and thermal (blue) energy confinement times versus B_T for the toroidal field scan at constant current, density and heating power.

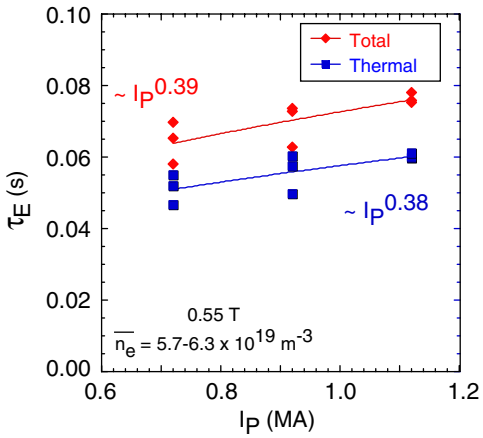

Figure 3. Total (red) and thermal (blue) energy confinement times versus I_p for the plasma current scan at constant toroidal field, density and heating power.

high plasma current (I_p up to 1.5 MA). The neutral beams heat the electrons preferentially, as is expected for α-heating in ITER, by approximately a 2 : 1 ratio. The large range of accessible β_T allows for exploration of turbulence spanning both electrostatic and electromagnetic regimes. The low toroidal field and large neutral beam induced rotation give rise to high levels of rotational shear that can influence transport. Finally, the low toroidal field results in a relatively large electron gyroradius ($\rho_e \sim 0.1$ mm), which allows electron scale turbulence to be measured locally. Thus, the NSTX is an excellent laboratory to study electron physics, and it can address fundamental transport and turbulence issues that are critical to both basic toroidal confinement and future devices, such as the ITER and the CTF [3]. Indeed, the NSTX data have been previously used along with MAST and START data and, in conjunction with higher aspect ratio data, to refine both the aspect ratio and the β_T dependence of confinement, for which these data have high leverage [4].

Confinement and transport studies have been carried out in MAST, another low aspect ratio tokamak with parameters and performance similar to those of the NSTX. Confinement studies of H-mode plasmas in MAST have shown the data to be broadly consistent with the ITER98PB(y,2) scaling [5], although with a stronger collisionality dependence than that indicated by this scaling [6]. Local transport analyses of the MAST discharges indicated that the ion thermal transport was close to the neoclassical level [7], consistent with early results on the NSTX as well [8]. Microinstability analyses with linear gyrokinetic codes indicated that the $E \times B$ shearing rates in MAST were sufficiently high so as to suppress long-wavelength ion temperature gradient (ITG) turbulence. The source of the anomalous electron transport was believed to be either microtearing modes in the core or radial streamers associated with saturated electron temperature gradient (ETG) turbulence [7, 9].

The purpose of this study is to address both the global confinement and local transport properties of the NSTX plasmas. This will be studied through results of dedicated scans primarily in H-mode plasmas, coupled with turbulence measurements and both linear and non-linear turbulence simulations. Since the past two years, the NSTX has implemented two key diagnostics; the first being a tangential microwave scattering system capable of measuring turbulence locally (± 3 cm) over a k_r from 2 to 25 cm^{-1}, covering the upper end of the ITG/TEM up through the ETG mode range [10]. Second, a 12-point motional Stark effect diagnostic, which measures the magnetic field pitch, allows the local transport properties to be related to details of the q-profile. In addition to these new diagnostics, the 20-point Thomson scattering (MPTS) system for measuring the electron temperature and density and the 51-point charge-exchange recombination spectroscopy (CHERS) diagnostic for measuring the carbon impurity profiles, ion temperature and toroidal rotation velocity provide the basis for determining the thermal confinement and local transport properties of the NSTX plasmas.

In the following sections we will present results from the global confinement scaling studies, followed by inferences of the local transport for both the ions and the electrons. The confinement and local transport studies will then be tied to

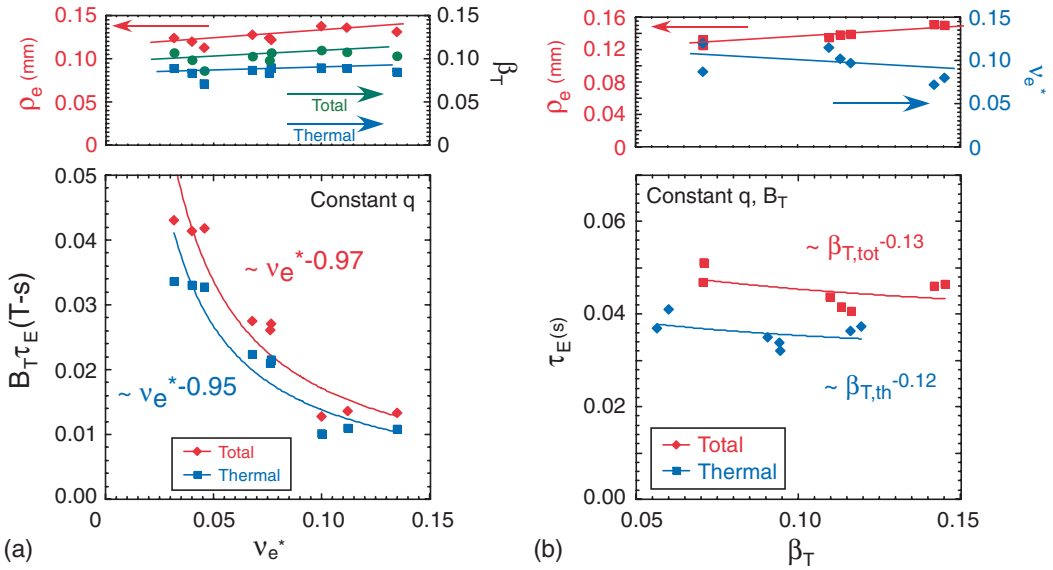

Figure 4. (*a*) Results of the collisionality scan in which attempts were made to hold ρ_e and β_T fixed. The variation of the latter two parameters over the range of ν_e^* is shown in the top panel, while the total (red) and thermal (blue) confinement times versus collisionality are shown in the bottom panel. (*b*) Similar to (*a*) but for the β_T scan.

both measurements of high-k turbulence and results of linear and non-linear turbulence/transport calculations in an attempt to understand the root cause of the transport in the NSTX. It is found that while the ion transport is at or near neoclassical levels, the electron transport is anomalous. Microtearing and ETG modes appear to be candidates for the electron transport under certain conditions.

2. Confinement scaling

Initial studies utilizing results from both systematic scans and statistical methods indicated that the global and thermal H-mode confinement times on the NSTX exhibited a stronger dependence on the toroidal magnetic field and a weaker dependence on the plasma current than did the data from devices at conventional aspect ratio [11]. In these studies, the H-mode τ_E (either global or thermal) scaled generally as $I_p^{0.6} B_T^{1.0} n_e^{0.35} P_L^{-0.60}$, where $P_L = P_{NBI} + P_{OH} - P_{loss} - dW/dt$, where $P_{loss} = P_{st}$ for the global confinement time and where $P_{loss} = P_{st} + P_{bo} + P_{cx}$ for the thermal confinement time, with the individual fast ion loss channels corresponding to shine-through (st), bad orbit (bo) and charge-exchange (cx) losses, respectively. When transformed into dimensionless physics variables, this scaling exhibits virtually no degradation of $B\tau_E$ with β_T, an important consideration for the success of the ITER advanced operating regime. In this set of data, the electrons were the dominant loss channel with the ion transport near neoclassical levels, and the improvement in confinement with increasing toroidal field was associated with primarily a decrease in transport in the electron channel.

Because of the difference in parametric dependences between the NSTX data and those at higher aspect ratio, it was found that the ITER98PB(y, 2) scaling [5] did not adequately describe the NSTX confinement times, generally overpredicting the ensemble of confinement data. This was seen quite clearly when the confinement enhancement factor of

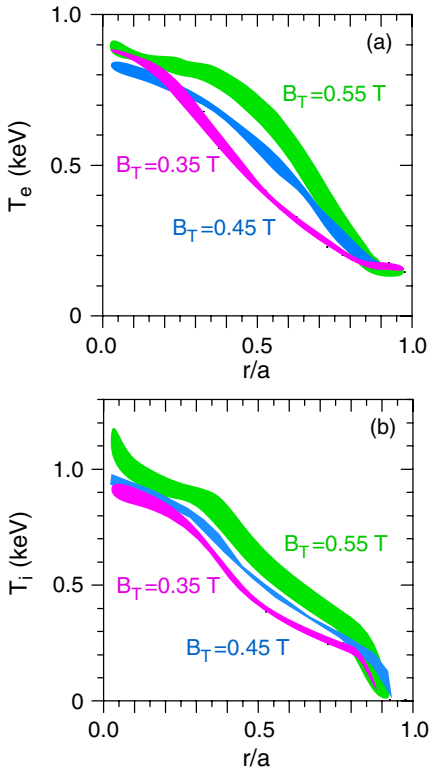

Figure 5. (*a*) Electron and (*b*) ion temperature profiles for the B_T scan at $I_p = 0.7$ MA and $n_e = (5.3–5.8) \times 10^{19}$ m^{-3}. Several shots at each B_T were taken, and the thickness of each profile represents the envelope of the individual profiles for that specific condition.

the ITPA H-mode database, with close to 90 NSTX datapoints contributed, was plotted versus the inverse aspect ratio [4]. The NSTX data, along with data from the low aspect ratio MAST and START devices and the standard selection set of higher aspect ratio data [12], were used to derive modified scalings. Furthermore, the greater range of β_T and $\epsilon (= a/R)$ provided

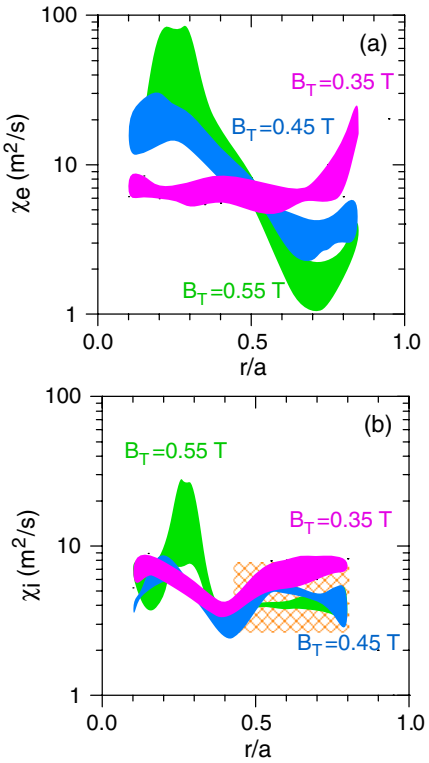

Figure 6. (*a*) Electron and (*b*) ion thermal diffusivity profiles for the B_T scan. The brown cross-hatched region indicates the level of neoclassical transport as calculated by GTC-NEO.

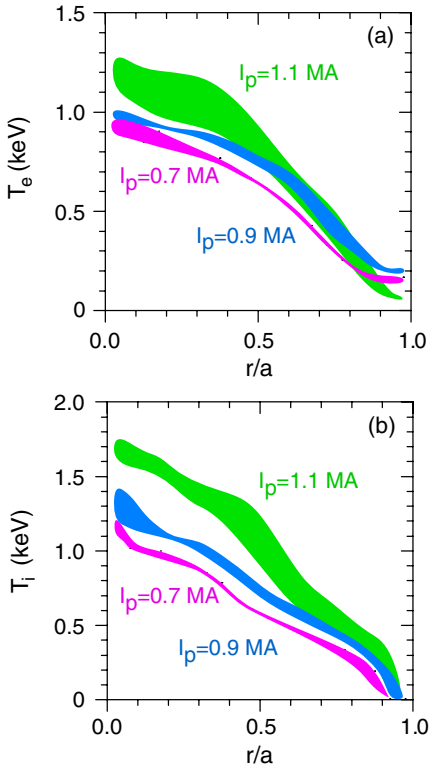

Figure 7. (*a*) Electron and (*b*) ion temperature profiles for the I_p scan at $B_T = 0.55$ T and $n_e = (5.7–6.3) \times 10^{19} m^{-3}$.

by the low aspect ratio data allowed for the determination of confinement scaling with these parameters to a higher degree of confidence. This analysis resulted in a scaling that described the full range of data better than done by the ITER98PB(y,2) and specifically resulted in a stronger scaling with inverse aspect ratio ($\tau_E \sim \epsilon^{1.03}$ versus $\epsilon^{0.58}$ as in 98y,2) and a weaker degradation with β_T ($B\tau_E \sim {\beta_T}^{-0.5}$ versus ${\beta_T}^{-0.9}$ as in 98y,2). The impact of the NSTX data was also to slightly reduce the dependence on the plasma current and increase the dependence on the toroidal magnetic field.

One of the issues in the NSTX dataset used for the above studies was a significant correlation among various engineering variables, most notably between line-averaged density and either plasma current or heating power. Consequently, dedicated scans were recently undertaken in an attempt to break this correlation and determine the parametric dependence on both B_T and I_p to a greater degree of certainty. For these scans, barely lower single null discharges with elongations κ of 2.1 and triangularities δ of 0.6 were run at constant injected beam power of 4 MW. Scans of toroidal field (0.35–0.55 T) were performed at fixed I_p of 0.7 and 0.9 MA, and an I_p scan was performed at $B_T = 0.55$ T. Scans at lower toroidal field or higher current resulted in discharges exhibiting large low-n MHD activity due to q-limits. The plasma densities in the discharges were comparable, allowing the confinement dependences on B_T and I_p to be isolated and determined individually. A scan was also performed at fixed q by varying B_T and I_p in tandem, keeping B_T/I_p fixed, as were individual scans of the dimensionless parameters β_T and ν_e^* (electron collisionality), while attempting to hold other dimensionless variables, including ρ_e, toroidal velocity shear and q, constant. These scans were completed in an efficient manner while being constrained by limited run time by taking advantage of the real-time EFIT control algorithm [13, 14] which held the plasma shape constant through all the parameter variations.

An overview of the B_T scan at $I_p = 0.7$ MA is shown in figure 1 where the toroidal field, the density and D_α are plotted from the top for discharges at 0.35 T, 0.45 T and 0.55 T, respectively. As can be seen from the D_α traces, all the discharges were in the H-mode with small ELMs only. The plasma density for all three toroidal fields track each other well, allowing a direct comparison among the discharges at constant beam power, density and plasma current. The normalized beta values for these discharges reach a maximum of 5.4, which is just below the ideal wall stability limit [15]. The total fast ion losses due to classical processes (shine-through, bad orbits and charge-exchange) varied from 13% to 20% for the three toroidal fields.

The scaling of both the thermal and the global confinement times as a function of toroidal field is shown in figure 2. Here the thermal and the global confinement times are defined as $\tau_{E,th} = W_{th}/P_L$ where $P_L = P_{NBI} + P_{OH} - P_{loss} - dW/dt$, P_{loss} includes shine-thru, bad-orbit and charge-exchange losses, and $\tau_{E,G}=(W_{th} + W_{fast})/P_L$, with W_{th} being the stored energy in the thermal plasma and W_{fast} the stored energy in the fast ion population. The core radiation is not subtracted out in determining P_L, consistent with what is typically done for the international H-mode confinement database. In the NSTX, the fraction of the volume-integrated radiation to the volume-integrated electron heating power in the core of the plasma ($r/a \leqslant 0.7$) is less than 10%. The confinement times

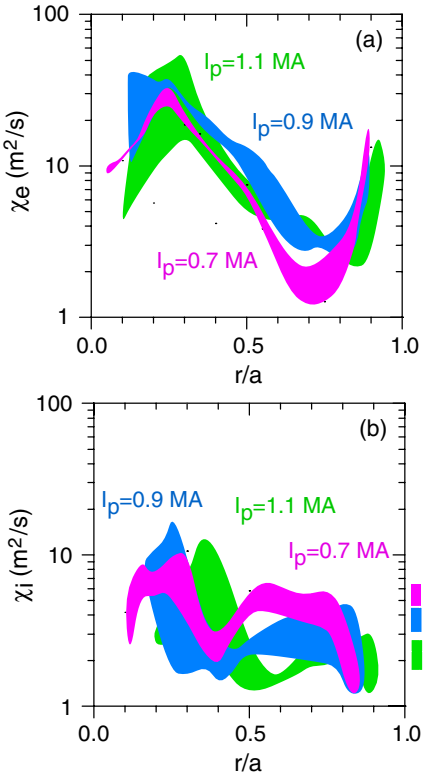

Figure 8. (*a*) Electron and (*b*) ion thermal diffusivity profiles for the I_p scan. The colour coded rectangles to the right of the figure are the neoclassical χ_i level for $r/a = 0.5$–0.8 for the three plasma currents, as computed by GTC-Neo.

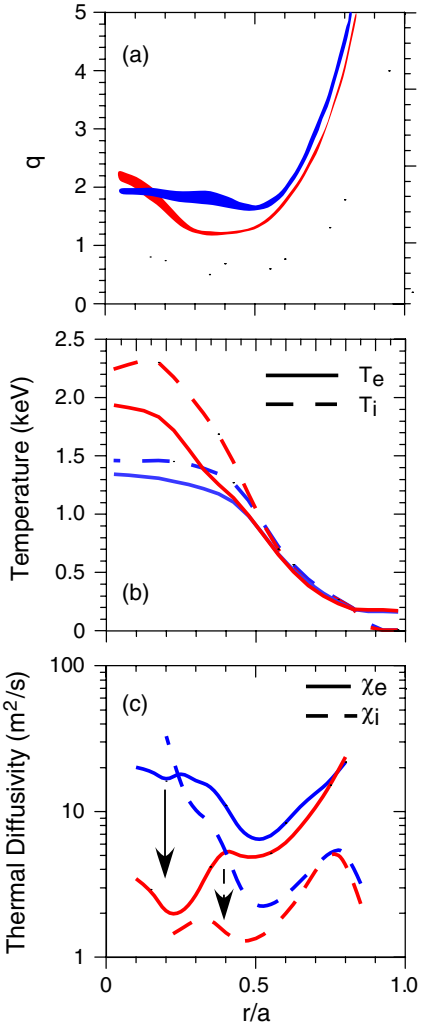

Figure 9. (*a*) q-profile comparisons for discharge with low central magnetic shear (blue) and strong reversed magnetic shear (red). (*b*) Electron (solid) and ion (dashed) temperature profiles for discharges shown in (*a*). (*c*) Electron (solid) and ion (dashed) thermal diffusivities for the discharges shown in (*a*).

clearly show a strong dependence on the toroidal field, with $\tau_{E,th} \simeq B_T^{0.91}$ and $\tau_{E,G} \simeq B_T^{0.85}$, which is a stronger dependence than then observed at a higher aspect ratio ($\tau_{E,th} \sim B_T{}^{0.15}$ in the ITER98PB(y,2) scaling). A similar toroidal field scan was performed at 0.9 MA, although the lowest toroidal field accessed was 0.4 T. Below that field, the discharges at 0.9 MA exhibited growth of large-scale low-n MHD activity. For the 0.9 MA scan, both the thermal and global confinement times scaled as $B_T^{0.6}$, slightly weaker than that at the lower current.

In contrast to the strong toroidal field dependence, the dependence of confinement on plasma current is weaker. This is seen in figure 3, where the results of a current scan from 0.7 to 1.1 MA at 0.55 T are shown. Both the thermal and global confinement times scale as approximately $I_p^{0.4}$ at a constant toroidal field, in contrast to the $I_p{}^{0.93}$ dependence in the ITER98PB(y,2) scaling. Data from the individual I_p and B_T scans combined, along with data from the constant q scans, indicate that at fixed q (fixed B_T/I_p), τ_E scales as $I_p{}^{1.3-1.5}$ (or equivalently $B_T{}^{1.3-1.5}$), stronger than the $I_p{}^{1.1}$ (or $B_T{}^{1.1}$) dependence at fixed q in the ITER98PB(y,2) scaling.

Dimensionless parameter scans to investigate the dependence of confinement on both ν_e^* and β_T were performed at constant q. The dependence of collisionality was obtained by varying both the toroidal field, along with the plasma current, and the plasma density. The results are shown in figure 4(*a*). The top part of the figure shows β_T and ρ_e as ν_e^* was varied, and while there was a factor of three variation in ν_e^*, there was only a 20% variation in the other parameters. The variation of Bτ_E with ν_e^* is strong, going as approximately ν_e^{*-1} (confinement improving as the discharge gets deeper into the trapped electron regime). This is in contrast to the $\nu_e^{*-0.4}$ dependence seen at a higher aspect ratio [12]. The result for the β_T scaling is shown in figure 4(*b*). Here, the β_T variation was accomplished by varying the density and the input power at a constant toroidal field (and constant q). ν_e^* and ρ_e varied only 20% over the range of the β_T variation, which was about a factor of 2.5. The confinement times degrade only weakly with β_T, going as $\beta_T{}^{-0.10}$. These results are consistent with the weak β_T scaling observed in dedicated JET and DIII-D scans [16, 17].

To investigate the influence of the slight ρ_e and β_T variation on the ν_e^* dependence, and the slight ρ_e and ν_e^* variation on the β_T dependence, a sensitivity study was undertaken. In this study, the β_T dependence of $B\tau_E$ was determined from the dataset for fixed chosen ρ_e and ν_e^* dependence, with these dependences being varied systematically. Using the results from 'good fits' only ($R^2 \geqslant 0.50$), a range of possible ν_e^*, β_T dependences was determined. Here, R^2 is defined as $R^2 = \sum(\hat{y}_i - \bar{y})^2 / \sum(y_i - \bar{y})^2$ where

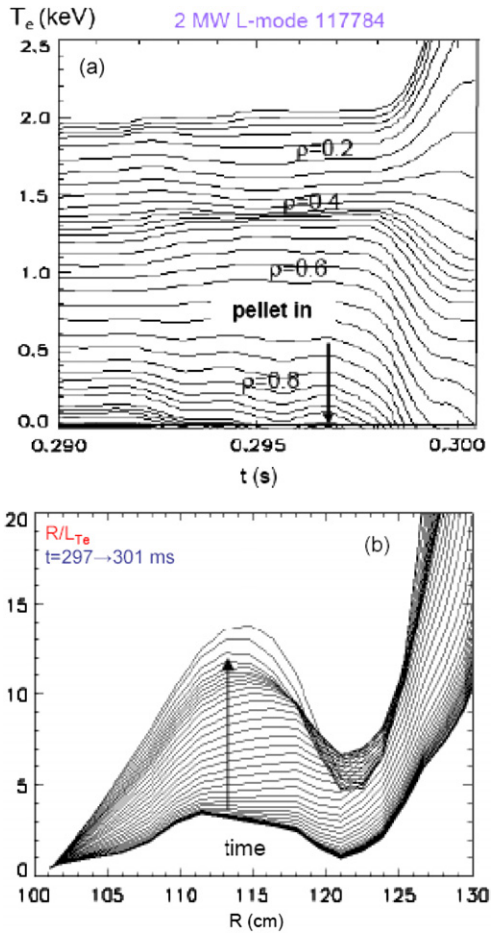

Figure 10. (*a*) Time evolution of SXR emissivity from a vertical array after a small lithium pellet was injected at 0.297 ms into an L-mode discharge with reversed magnetic shear and an eITB. (*b*) Evolution of R/L_{T_e} profiles for 4 ms after the pellet injection.

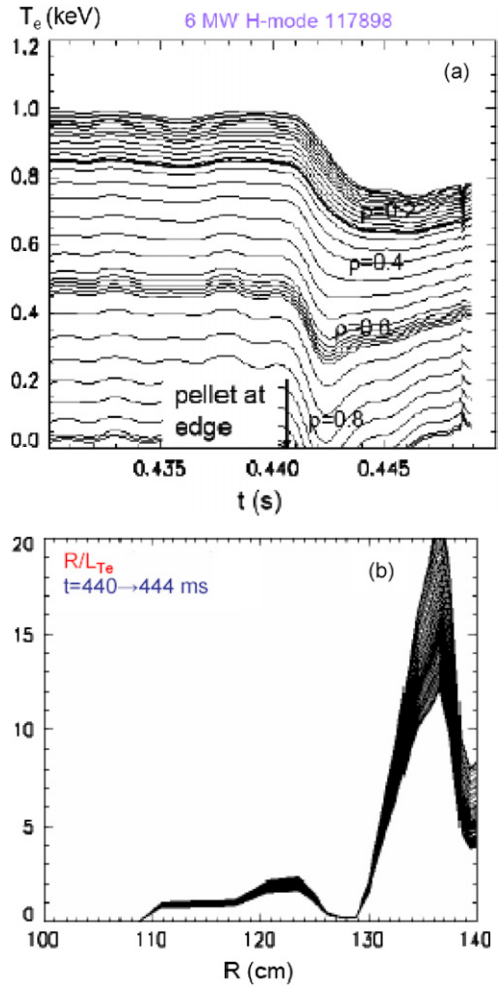

Figure 11. (*a*) Time evolution of SXR emissivity from a vertical array after a small lithium pellet was injected at 0.440 ms into an H-mode discharge with reversed magnetic and low central magnetic. (*b*) Evolution of R/L_{T_e} profiles for 4 ms after the pellet injection.

y_i are the datapoints, $\bar{y}$ is the average of the data and $\hat{y}_i$ are the values predicted by the fit. The ρ_e dependence was varied from $B\tau_E = \rho_e^{-2.0\ to\ -4.0}$, but good fits were obtained only when the coefficient was in the gyroBohm range, from -2.5 to -3.5. For this range of ρ_e dependence, the range of ν_e^* and β_T dependences was found to be $B\tau_E \sim \nu_e^{*(-0.5\ to\ -0.9)}\beta_T{}^{0.2-0.4}$, with an inverse relation between the ν_e^* and the β_T coefficients (i.e. the β_T coefficient decreases towards zero as the absolute value of the ν_e^* coefficient increases). This statistical approach to determining the range of coefficients has some inherent uncertainty in that the ρ_e, ν_e^* and β_T values are correlated (through their definitions, all of which contain T_e and B_T, in addition to n_e being common to both ν_e^* and β_T). This leads to correlations between the scaling coefficients for these parameters.

3. Local transport results

In this section, the local transport properties governing the B_T and I_p confinement scalings discussed above will be investigated. The role that the q-profile plays in the controlling of the local temperature gradient and transport will also be discussed. The electron and ion temperature profiles for the three toroidal fields in the 0.7 MA B_T scan are shown in figures 5(*a*) and (*b*). The coloured band for each toroidal field represents the envelope of profiles measured for that condition (i.e. several discharges at each condition were produced to study reproducibility). It is clearly seen that as the toroidal field increases the electron temperature profile broadens considerably, while the central temperature remains approximately constant. This behaviour is very different from what was observed at a higher aspect ratio, where it was the central T_e that was most affected by variations in the toroidal field [18]. The ion temperature profiles, on the other hand, show less variation with B_T. For all the discharges in this scan, the density profiles essentially overlaid each other.

Transport analysis of these discharges was done using the TRANSP analysis code [19, 20], which uses measured temperature and density (including impurity) profiles, rotation velocity and radiated power, and it computes the beam ion deposition and density using a Monte-Carlo approach to determine the sources and losses of energy and particles. From these terms, the local particle and thermal diffusivities are calculated. For these calculations, the neutral beam ions were assumed to behave classically, consistent with the agreement found between the measured neutron rate and

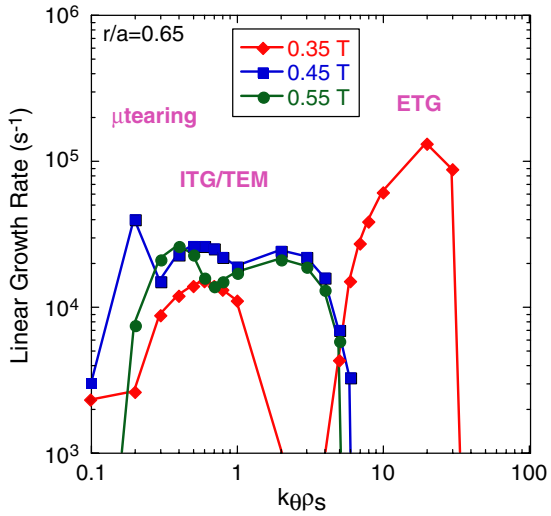

Figure 12. Linear growth rates as a function of $k_\theta \rho_s$ for three discharges in the B_T scan as computed by GS2.

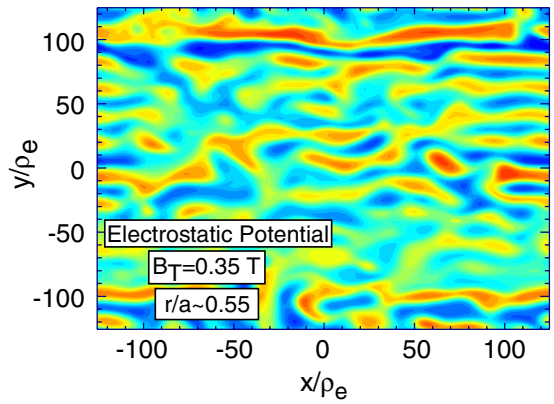

Figure 13. Results from a non-linear fluid calculation with finite Larmor radius corrections of the 0.35 T discharge at $r/a = 0.55$. The calculation shows the formation of radial streamers with radial extents of $200\rho_e$ (~2 cm).

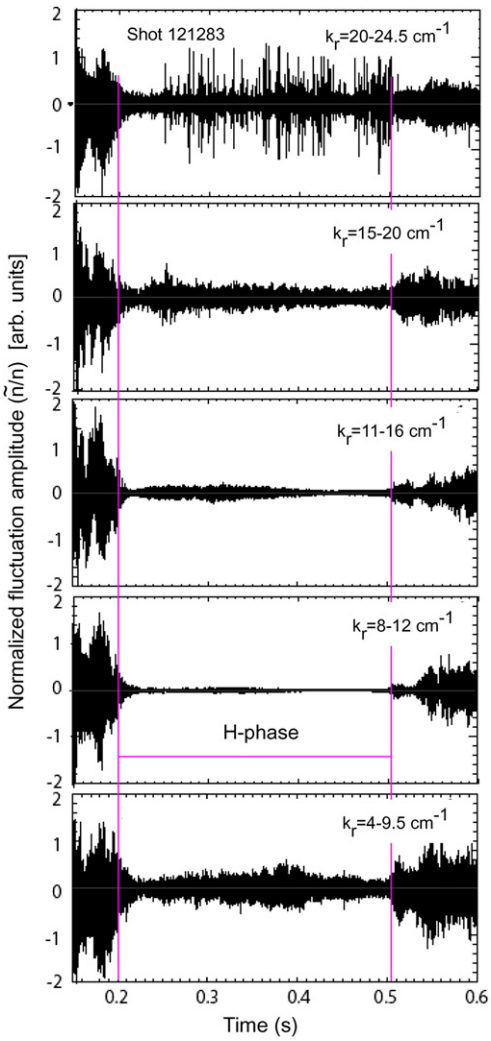

Figure 14. Normalized density fluctuation amplitudes $\tilde{n}_e/n_e$ as a function of time for a discharge that transitioned from the L- to the H-mode, and then back to the L-mode. The density fluctuations were measured by a tangentially viewing microwave scattering diagnostic. The diagnostic measures k_r from the upper ITG/TEM range up to the ETG range.

the neutron rate calculated assuming no anomalous fast ion loss or redistribution due to MHD activity. While some of the discharges in this study exhibited Alfvén eigenmode activity, the level of activity, when present, was low compared with levels known to lead to fast ion redistribution or loss. In addition, there was virtually no MHD activity at frequencies greater than $f_c/2$. Theoretical work suggested that compressional Alfvénic modes in this frequency regime with significant amplitudes ($\delta B/B \geqslant 5 \times 10^{-3}$) could potentially lead to stochastic heating of thermal ions [21].

The electron thermal and ion thermal diffusivities for the discharges in the B_T scan are shown in figures 6(*a*) and (*b*). Apparent in figure 6 is that it is the electron thermal diffusivity that varies the most as the toroidal field is varied. As can be seen in figure 6(*a*), the χ_e decreases significantly outside $r/a = 0.5$ as the toroidal field increases, consistent with the broadening of the electron temperature profile with the increasing toroidal field. The χ_e profiles exhibit a pivot point around $r/a = 0.5$; inside this radius the χ_e increases with increasing toroidal field, which is primarily due to an increased flattening of the T_e profile in this region with higher B_T. The higher χ_e in this low volume core region has a minimal effect on the electron or thermal confinement increase with B_T, which is apparently controlled more by the transport outside $r/a = 0.5$. The large χ_es in the core, where the temperature gradient drive term is small, may be due to non-local effects such as turbulence spreading [22]. The ion thermal diffusivity changes very little with B_T, as can be seen in figure 6(*b*), and the inferred χ_i values are within the range of the ion neoclassical transport coefficients as determined by GTC-NEO [23], which takes into account finite banana width and thus non-local effects. The neoclassical range in the region outside $r/a = 0.5$ is indicated by the brown cross-hatched region. Beyond $r/a = 0.5$, $\chi_i > \chi_e$ at the higher B_T.

In contrast to the B_T scaling results, it is more the ions than the electrons that control the variation of confinement in the I_p scan. The electron and ion temperature profiles from the I_p scan at $B_T = 0.55$ T are shown in figures 7(*a*) and (*b*), respectively. A 20–30% increase in the central electron

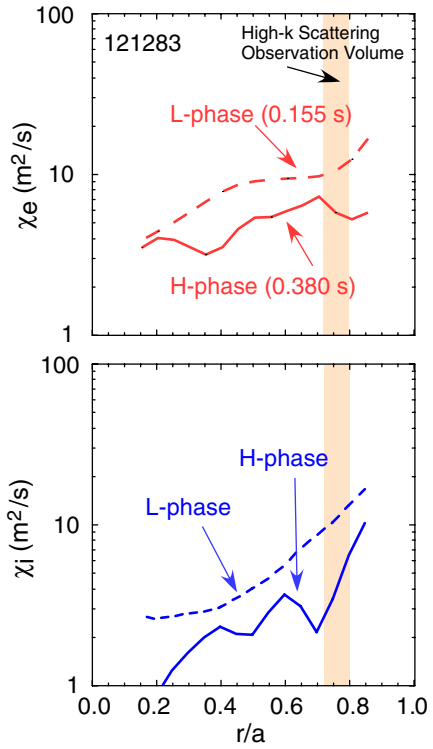

Figure 15. Electron (top panel) and ion (bottom panel) thermal diffusivities for the early L- (dashed curve) and H- (solid curve) phases of the discharge shown in figure 14. The ion thermal diffusivity is near the neoclassical level during the H-phase.

temperature is seen as the plasma current increases from 0.7 to 1.1 MA (mostly going from 0.9 to 1.1 MA), although there is no change in T_e outside $r/a = 0.4$. The change in T_i with plasma current is stronger, with a 55% change in the central T_i from the lowest to the highest current, with the increase seen to be out to $r/a = 0.6$. The ion temperature profile shapes remain essentially the same for all currents; there is no broadening as was seen for T_e with increasing toroidal field.

In figures 8(*a*) and (*b*) the electron and ion thermal diffusivities are plotted for the three different currents in the I_p scan at $B_T = 0.55$ T. As can be seen in figure 8(*a*), χ_e changes only slightly as the plasma current is increased, while, in figure 8(*b*), χ_i decreases with increasing current outside $r/a = 0.4$, but it changes very little inside that radius. As was the case for the B_T scan, the ion transport is near the neoclassical level. The neoclassical level here is also determined by GTC-NEO. The neoclassical χ_i ranges for the three current levels, in the regions from $r/a = 0.5$–0.8, are indicated by the colour coded rectangles at the right of the figure. As can be seen, the χ_is inferred from experimental measurements in the region from $r/a = 0.5$ to 0.8 are at the neoclassical level for all three currents. It is the change in $\chi_{i,neo}$ with the plasma current that underlies the change in overall confinement with I_p. It is also seen that $\chi_e < \chi_i$ at the lowest current.

In addition to the dependences of the inferred transport coefficients on the global discharge parameters, the local transport characteristics are found to be also dependent on local parameters such as the magnetic shear. A set of experiments in low density L-mode plasmas was carried out to study this effect utilizing the 12-point MSE diagnostic for an accurate reconstruction of the current profile. The magnetic shear in these plasmas was controlled by adjusting both the onset time of the neutral beam heating and the plasma current ramp rate to, in turn, control the MHD activity in the early phase of the discharge. The reconstructed q-profiles for a set of comparison shots, one with a weak central magnetic shear and one with a strongly reversed central magnetic shear, is shown in figure 9(*a*). While the MHD activity differed in the early phase of these discharges, there was no MHD activity in either discharge at the times of interest, which were chosen when the density was the same. The electron temperature profile for the strongly reversed shear case is peaked, exhibiting an electron internal transport barrier (eITB) at the location of q_{min}. The ion temperature profile for the reversed shear discharge also exhibits peaking in the same region (figure 9(*b*)). Both the electron and the ion thermal diffusivities are lower in the reversed shear discharge than in the low central shear discharge most notably inside the region bounded by the q_{min} of the reversed shear discharge (figure 9(*c*)). Within this region, there is a factor of 3–10 difference in both χ_e and χ_i between the two discharges [24].

Perturbative studies using lithium pellets and the soft x-ray array (SXR) to diagnose fast changes in the electron temperature also showed the influence of the q-profile on plasma temperature gradients and transport. Figure 10(*a*) shows the time history of the SXR channels across the plasma in a reversed shear L-mode discharge with an eITB, in which a small lithium pellet was injected at $t = 0.297$ s. Ths SXR emission responds slowly to the pellet perturbation, changing on a time scale of several ms. The computed R/L_{T_e}, shown in figure 10(*b*), also exhibits a slow response and a continual increase in the T_e gradient after pellet injection. In contrast to this, an H-mode plasma with a monotonic q-profile exhibits a rapid change in the SXR emissivity across the entire profile (figure 11(*a*)), but no change in R/L_{T_e} (figure 11(*b*)) following the pellet perturbation. This indicates stiff profiles in the monotonic q-case and the possible existence of a critical temperature gradient.

4. Theory calculations and turbulence measurements

In this section, theory calculations and turbulence measurements are used to identify, and to develop an integrated picture of, the possible sources of anomalous electron transport and its trends in the NSTX plasmas. As shown in the previous section, it is the variation in electron transport that is primarily responsible for the strong confinement dependence on B_T. Linear gyrokinetic and non-linear fluid simulations have been used to identify the source of the change in transport levels in the B_T scan. Linear growth rates computed by GS2 [25] for the discharges in the $I_p = 0.7$ MA, B_T scan are shown in figure 12 as a function of $k_\theta \rho_s$ at a radius of $r/a = 0.65$, where the sharp decrease in χ_e with increasing B_T is observed. This calculation determines the linear growth rate of only the fastest growing mode. It is seen in figure 12 that long wavelength modes are linearly unstable with comparable growth rates for all the three toroidal field levels. These long-wavelength modes show characteristics of both microtearing and hybrid ITG/TEM modes from the mode structures and

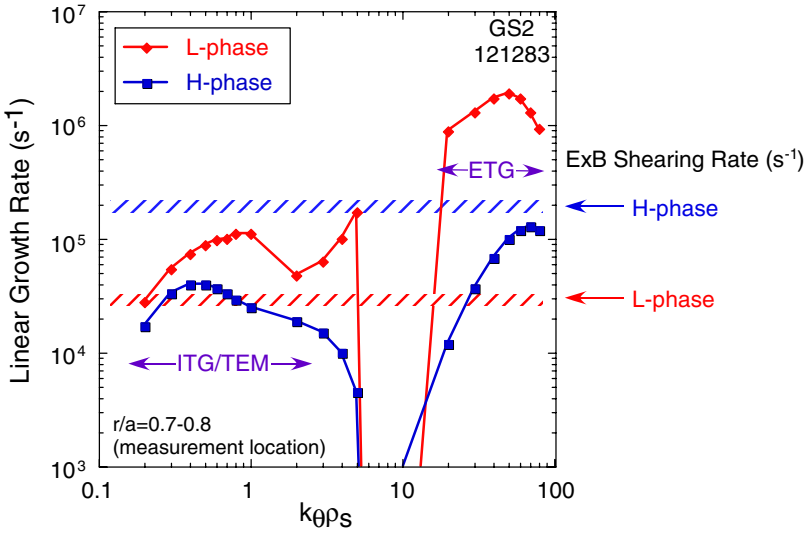

Figure 16. Linear growth rates as a function of $k_\theta \rho_s$ for the first L-mode phase and the H-phase of the discharge shown in figure 14. Also shown are the $E \times B$ shearing rates for both phases.

propagation direction. At 0.35 T, however, the range of $k_\theta \rho_s$ for which these longer wavelength modes are unstable is narrower than at the higher two toroidal field levels, and a stable region is seen for $k_\theta \rho_s$ between one and four. At shorter wavelengths for this, and only for this toroidal field, the ETG mode is predicted to be unstable, with γ_{lin} greater by a factor of 5–10 than at lower $k_\theta \rho_s$. For the 0.35 T case, the measured ETG is approximately 20% greater than the critical value for driving ETG modes unstable, while at the higher toroidal fields, the T_e gradients are 20–25% below the critical value.

The potential importance of ETG modes in determining the electron transport at $B_T = 0.35$ T has also been indicated by results from a non-linear FLR-modified fluid code [26]. The electrostatic potential in the saturated state is plotted in figure 13 for $r/a = 0.55$, and the formation of streamer-like structures with a radial extent of up to $200\rho_e$ ($\sim$2 cm) is clearly seen. The radial streamer structures play a role in enhancing heat transport, and they yield an upper bound for the heat flux by the ETG turbulence. The computed saturated electron heat flux due to the ETG and these structures is approximately 100 kW m^{-2} , while the value inferred by TRANSP is between 100 and 130 kW m^{-2}, consistent with the non-linear calculation. Additional non-linear calculations indicate the ETG mode to be stable at both 0.45 and 0.55 T, in agreement with the linear results.

A diagnostic recently implemented on the NSTX is a tangential microwave scattering system capable of measuring density fluctuations from approximately $k_r = 2$ to 25 cm^{-1} [10]. This spans the upper ITG/TEM up to the ETG range of wavenumbers. The diagnostic is radially scannable, and it can measure the fluctuations from near the magnetic axis to out near the edge of the plasma. Furthermore, the diagnostic has an unrivalled spatial resolution of $\pm$3 cm. Figure 14 shows a time history of normalized fluctuation levels ($\tilde{n}_e/n_e$) for $k_r = 4$–24 cm^{-1} as measured by this system for a 2 MW discharge that transitioned from the L-mode to the H-mode at 0.2 s and then backtransitioned to the L-mode at 0.5 s. The measurements were localized to a radius from $r/a = 0.7$ to 0.8 during the course of the discharge. The range of k_r values given for each channel is due to refraction effects owing to different densities and density profiles between the L- and H-phases. The lower k_r for each channel reflects the measurement during the L-phase, while the upper value reflects that during the H-phase. What is clear in the figure is that the fluctuation levels decrease for all k_r going from the L-mode to the H-mode, and they increase as the discharge backtransitions into the L-mode. The spikes seen in the highest k_r channel are coherent electrostatic bursts that are associated with ELMs, and they are the subject of another study. Associated with the decrease in fluctuation level during the H-mode is a factor of 3–10 reduction in both the electron and ion thermal diffusivities going from L to H (figure 15). The electron transport is anomalous for both phases, but the ion transport is close to the neoclassical level during the H-phase. $\chi_e > \chi_i$ during both the L- and H-phases for this discharge.

Linear GS2 calculations have been performed to try to identify the source of the turbulence and its reduction. The linear growth rates and $E \times B$ shearing rates based on the Hahm–Burrell formulation [27] for the early L-phase and the H-phase calculated at the turbulence measurement location are plotted in figure 16 as a function of $k_\theta \rho_s$. Both the ITG/TEM and ETG modes are calculated to be linearly unstable during the L-phase, with growth rates which exceed the $E \times B$ shearing rate by at least a factor of several for the entire wavenumber range. As the discharge transitions into the H-phase, and the calculated electron and ion transport decrease, the linear growth rates also decrease for all $k_\theta \rho_s$. Furthermore, the linear growth rate in the ITG/TEM range is much less than the $E \times B$ shearing rate. Non-linear global GTC calculations indicate that ITG modes are stable during the H-phase of the discharge. The results of both calculations are consistent with stabilization of this low-k mode and the computed ion transport falling to near neoclassical levels. The linear growth rates in the ETG regime are slightly below the $E \times B$ shearing rate, and just how this shearing rate affects the growth of these small-scale ETG modes is a topic that will be addressed through self-consistent non-linear calculations. The inferred χ_e profile shapes for both the L- and the H-phases agree with those from an analytic formulation of the electrostatic

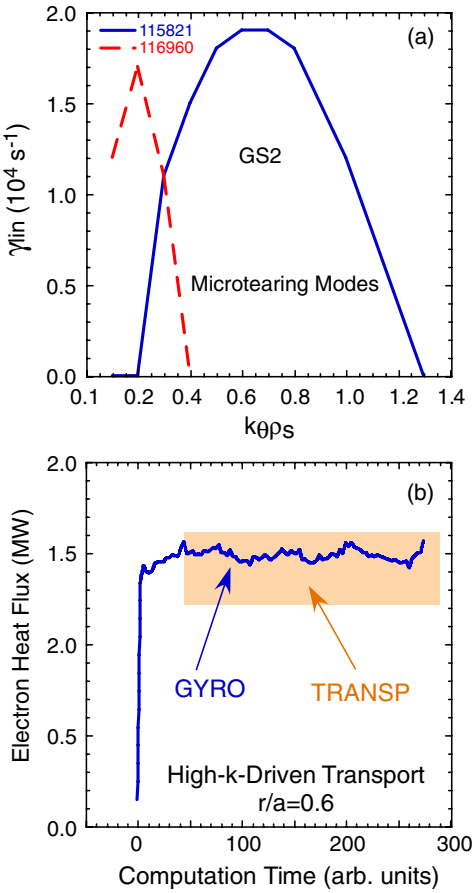

Figure 17. (*a*) Linear growth rates from GS2 as a function of $k_\theta \rho_s$ for the weak magnetic central shear discharge (blue) and strongly reversed magnetic shear discharge (red) showing the difference in the range of unstable microtearing modes at $r/a = 0.28$. (*b*) Time history showing the saturation of the non-linear electron heat flux driven by ETG modes as computed by GYRO at $r/a = 0.6$ for the strong magnetic shear case. The brown shaded region indicates the range of electron heat flux values inferred from transport analysis (TRANSP) for $r/a = 0.55$–0.65. The results for the weak magnetic shear discharge at this radius are similar.

ETG [28] (for this plasma, β_T at $r/a = 0.7$–0.8 was 1% and 3% for L- and H-modes, respectively).

Finally, it is noted that both linear and non-linear analyses have been performed on the weak versus reversed magnetic shear discharges shown in figure 9. In the region where the q-profiles differ significantly, $r/a \leqslant 0.3$, the results of linear GS2 calculations indicate that while the ITG, TEM and ETG modes are stable in that region, microtearing modes are not. The reduction in transport inferred in the reverse-shear discharge is associated with a reduced k_θ range over which the microtearing modes are unstable (figure 17(*a*)). Outside this region, where $r/a \simeq 0.6$, non-linear GYRO [29] indicate that ETG modes are unstable, and the calculated saturated electron heat flux value from these ETG modes is consistent with that inferred from transport analysis (figure 17(*b*)).

5. Summary and discussion

Experiments on the low aspect ratio, high β_T NSTX have explored the trends and sources of the variations in transport

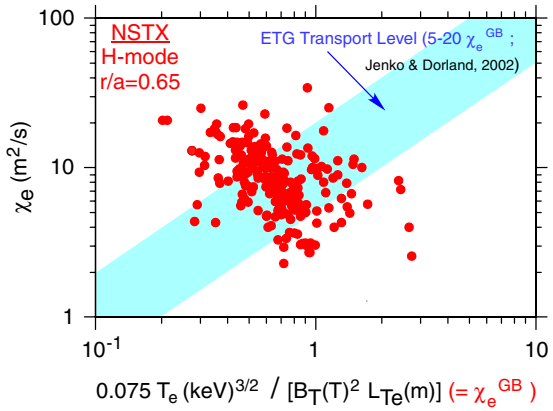

Figure 18. χ_e as a function of $\chi_{e,\mathrm{GyroBohm}}$ for a collection of the NSTX H-mode discharges at $r/a = 0.65$. The blue shaded region indicates the theoretically expected range of χ_e that would be consistent with ETG-driven transport (5–20 times $\chi_{e,\mathrm{GyroBohm}}$).

and turbulence across a range of operating conditions. The NSTX confinement shows a strong dependence on the toroidal field and a weaker dependence on the plasma current, which translates to an $I_p^{1.3-1.5}$ dependence at fixed q, stronger than that in the ITER98PB(y,2) scaling. Dedicated dimensionless parameter scans have shown a strong increase in confinement with decreasing collisionality, and only a very weak degradation with β_T, an important result for the success of the advanced operating scenario on the ITER. The local transport trends that give rise to these confinement variations have been studied, and it was found that while reduced electron transport resulted in the improvement in confinement with increasing B_T, it is the reduction in ion transport, closely coupled to neoclassical transport levels, that was responsible for the improvement with I_p. Transport characteristics were found to be sensitive to $q(r)$, with the formation of electron ITBs and non-stiff profiles associated with reversed magnetic shear.

Through measurements of density fluctuations from low- to high-k, and through linear and non-linear theoretical calculations, studies to determine the cause of the anomalous electron transport have begun. A decrease in the density fluctuation signal amplitude going from the L-mode to the H-mode was seen to be associated with a reduction in the inferred electron and ion transport. The ETG mode was found to be a candidate for the electron transport under certain conditions. In particular, ETG modes could be important for controlling the electron transport at the lowest toroidal field in the B_T scan. Furthermore, the change in the calculated linear ETG growth rates is associated with a reduction in the measured high-k_r turbulence and the inferred electron transport going from the L-mode to the H-mode.

A more statistical approach has also been taken to study the possible role of ETG modes in controlling the electron transport on the NSTX. This is shown in figure 18, where the inferred experimental χ_e is plotted against the gyroBohm electron diffusivity, $\chi_{e,GB}$, for a collection of the NSTX H-mode discharges at $r/a = 0.65$. The blue shaded region in the plot denotes the range of χ_e predicted by theory to result from ETG turbulence, which is 5–20 times $\chi_{e,GB}$ [30]. There is clearly a significant number of the NSTX discharges at this

level of χ_e. This is not, however, sufficient proof that ETG modes are the dominant source of electron transport, as there are also a significant number of points with higher χ_e, and, therefore, the role of lower-k modes has to be assessed as well. The results do suggest, however, that ETG modes cannot be ruled out.

Future work will focus on further assessing the turbulence characteristics as well as performing more comprehensive non-linear gyrokinetic simulations to identify the source(s) of the anomalous electron transport, and specifically the role of micro-tearing and ETG mode-induced transport, over a wide range of operating conditions.

Acknowledgments

This work was supported by the US Department of Energy Contract DE-AC02-76CH03073 at the Princeton Plasma Physics Laboratory, DE-FG02-99ER54518 at the UC Davis and DE-FG02-99ER54524 at the Columbia University. The authors would like to thank the entire NSTX operations, physics and engineering teams for their contributions to this effort.

References

[1] Kaye S.M. *et al* 2005 *Nucl. Fusion* **45** S168
[2] Bell M.G. *et al* 2006 *Nucl. Fusion* **46** S565
[3] Peng Y-K. M. *et al* 2005 *Plasma Phys. Control. Fusion* **47** B263
[4] Kaye S.M. *et al* 2006 *Plasma Phys. Control. Fusion* **48** A429
[5] ITER Physics Basis 1999 *Nucl. Fusion* **39** 2137
[6] Valovic M. *et al* 2005 *Nucl. Fusion* **45** 942
[7] Field A.R. *et al* 2004 *Fusion 2004: Proc. 2nd Fusion Energy Conf. (Vilamoura, Portugal)* Paper EX/P2-11
[8] Leblanc B.P. *et al* 2004 *Nucl. Fusion* **44** 513
[9] Roach C. *et al* 2005 *Plasma Phys. Control. Fusion* **47** B323
[10] Smith D.R. *et al* 2004 *Rev. Sci. Instrum.* **75** 38
[11] Kaye S.M. *et al* 2006 *Nucl. Fusion* **46** 848
[12] Cordey J.G. *et al* 2005 *Nucl. Fusion* **45** 1078
[13] Ferron J.R. *et al* 1998 *Nucl. Fusion* **38** 1055
[14] Gates D.A. *et al* 2006 *Nucl. Fusion* **46** 17
[15] Menard J.E. *et al* 2006 *Phys. Rev. Lett.* **97** 095002
[16] McDonald D.C. *et al* 2004 *Plasma Phys. Control. Fusion* **46** A215
[17] Petty C.C. *et al* 2004 *Phys. Plasmas* **11** 2514
[18] Kaye S.M. *et al* 1984 *Nucl. Fusion* **24** 1303
[19] Hawryluk R.J. 1979 *Physics of Plasmas Close to Thermonuclear Conditions: Proc. Course (Varenna)* vol 1 p 19
[20] Goldston R.J. *et al* 1981 *J. Comput. Phys.* **43** 61
[21] Gates D.A., Gorelenkov N.N. and White R.B. 2001 *Phys. Rev. Lett.* **87** 205003
[22] Hahm T.S. *et al* 2004 *Plasma Phys. Control. Fusion* **46** A323
[23] Wang W. *et al* 2004 *Comput. Phys. Commun.* **164** 178
[24] Levinton F.M. *et al* 2007 Transport with reversed shear in the national spherical torus experiment *Phys. Plasmas* at press
[25] Kotschenreuther M. *et al* 1995 *Comput. Phys. Commun.* **88** 128
[26] Horton W. *et al* 2005 *Nucl. Fusion* **45** 976
[27] Hahm T.S. and Burrell K. 1995 *Phys. Plasmas* **2** 1648
[28] Horton W. *et al* 2004 *Phys. Plasmas* **11** 2600
[29] Candy J. and Waltz R.E. 2003 *Phys. Rev. Lett.* **91** 045001
[30] Jenko F. and Dorland W. 2002 *Phys. Rev. Lett.* **89** 225001